Soft Matter

Effects of chain length and polydispersity on shear banding in simple shear flow of polymeric melts

Journal:	*Soft Matter*
Manuscript ID	SM-ART-04-2020-000669.R1
Article Type:	Paper
Date Submitted by the Author:	26-May-2020
Complete List of Authors:	Boudaghi-Khajehnobar, Mahdi; University of Tennessee Knoxville College of Engineering, Chemical and Biomolecular Engineering Edwards, Brian; University of Tennessee Knoxville College of Engineering, Chemical and Biomolecular Engineering Khomami, Bamin; University of Tennessee, Department of Chemical and Biomolecular Engineering

Effects of chain length and polydispersity on shear banding in simple shear flow of polymeric melts

Mahdi Boudaghi-Khajehnobar[1], Brian J. Edwards[1,*], and Bamin Khomami[1,*]

Abstract:

The characteristics of shear banding were investigated in entangled, polydisperse, linear polymer melts under steady-state and startup conditions of simple shear flow. This virtual experimentation was conducted using course-grained nonequilibrium dissipative particle dynamics simulations expressed in terms of a force-field representation that faithfully models the atomistic system dynamics. We examined melts with two mean molecular bead numbers of $N_n = 250, 400$ and polydispersity indexes of 1.025, 1.05. The wide range of relaxation timescales in the polydisperse melts decreased the nonmonotonic character of the steady-state shear stress vs. shear rate profile compared to a monodisperse linear melt. The polydispersity level required to observe a stress plateau in the shear stress profile at intermediate shear rates was correlated with the nominal entanglement density. Startup of shear flow simulations revealed the development of spatial inhomogeneities and dynamic instabilities in polydisperse fluids containing both monotonic and nonmonotonic shear stress flow curve. Although the shape and duration of instabilities were found to be correlated with the monotonicity of the shear stress profile, the onset and underlying mechanism leading to the formation of shear bands were generally universal. The simulations revealed that perturbations arose soon after the occurrence of a large stress overshoot under startup conditions, and that banded structures stemmed from local reorientation and subsequent deconstruction of the entanglement network. Furthermore, data indicated that the inception of strain localization occurred at shear rates near the reciprocal of the Rouse characteristic timescale, $\dot{\gamma} > {\tau_R}^{-1}$. Transient shear banding was observed in shorter chain melts undergoing startup of shear flow in which instabilities arose after the appearance of a stress overshoot. These instabilities eventually decayed, but only long after the stresses had attained their steady-state values. The longer chain melt exhibited a shear band structure that remained indefinitely, long after the stresses had attained steady state.

Keywords: Shear banding, Polydispersity, Polymer melts, Dissipative particle dynamics

[1] Materials Research and Innovation Laboratory (MRAIL), Department of Chemical and Biomolecular Engineering, University of Tennessee, Knoxville, TN, 37996, USA.

[*] Corresponding Author: bje@utk.edu; bkhomami@utk.edu

I. Introduction:

Industrial processing of polymeric solutions and melts is strongly impacted and limited by flow instabilities that occur at typical strain rates; indeed, final product characteristics are greatly influenced by the process flow history. Processed viscoelastic polymeric solutions and melts are prone to dynamic instabilities, metastable states, nonlinearities, and periodic chain tumbling. These nonlinear dynamics can manifest in a variety of ways, such as shear banding, stick-slip flow, sharkskin, extrudate distortion, polymer migration, flow hysteresis, *etc*. [1-3] These phenomena are rooted in the complex dynamic response of the system to process kinematics, which stimulate liquid response covering a vast range of time and lengths scales. The coupling of the inherent dynamic responses of individual relaxation modes over such large ranges can produce an inherently nonlinear and unstable response of the local fluid properties, which can translate into spatial inhomogeneities in the macroscopic response of the fluid to process flow history. Shear banding, in particularly, has been studied extensively in recent years, although its root causes and effects are still hotly debated [4-7]. Nevertheless, there remain many potential factors impacting the manifestation of shear banding that have yet to be examined, such as the effect of polydispersity of the sample molecular weight.

Many viscoelastic fluids, including polymer solutions, melts, wormlike micelles, and liquid crystalline polymers, exhibit shear banding. It is manifested in a sheared fluid as a strain rate localization where distinct domains within the liquid exhibit different strains or strain rates. Occurrence of shear banding has been traditionally associated with the negative slope of the steady-state shear stress flow profile $\left[{d\sigma_{xy}}/{d\dot{\gamma}}\right] < 1$, where σ_{xy} is the steady-state shear stress and $\dot{\gamma}$ is the shear rate. To this end, constitutive equations that can capture a non-monotonic flow curve, such as Johnson-Segalman [8, 9], are capable of capturing a banded velocity profile in simple shear flows. The original Doi and Edwards constitutive equation [10-12] gives rise to a nonmonotonic flow curve for a monodisperse entangled polymeric fluid with a stress maximum at $\dot{\gamma}^* = \tau_d^{-1}$, inverse of the disengagement time). However, new concepts have been introduced in advanced tube-based models [13-18] to eliminate the nonmonotonicity as they are not commonly observed in commercial, i.e., polydisperse, entangled polymeric fluids.

Shear banding was first observed in wormlike micelles (WLM) in the early 1990's [19, 20]. The first observation of transient (banded structure disappears once the flow reaches steady sate) and steady shear banding in entangled polymeric liquids was made in 2006 by Tapadia and Wang in step-strain startup of shear flow via particle tracking velocimetry [21]. These initial experiments were subsequently extended by Wang and coworkers to a host of polymeric fluids, including a well-entangled DNA solution (more than 40 entanglements per chain) in steady and oscillatory shear flows [22-25]. Wang and co-workers ascribed the occurrence of shear banding to an "elastic

yielding" and an "entanglement−disentanglement transition" of the polymer network [26]. The elastic yielding concept has been widely challenged in the polymer physics and rheology communities, as experimental studies have shown that banded velocity profiles can also be realized due to edge fracture. Moreover, Helgeson *et al*. have demonstrated flow-concentration coupling in a shear-banded fluid of wormlike micelles (WLM), and they have concluded that strain localization is associated with shear-induced de-mixing [27]. Alternatively, Gurnon *et al*. have observed a shear-induced anisotropic pattern in linear polymer-like micelle (PLM) solutions as an indication of flow alignment. Unlike Helgeson *et al*., Gurnon *et al*. have not observed significant concentration differences; therefore, they ascribed the observed shear banding to the coexistence of an aligned and more-entangled PLM layer [28].

Olmsted, Fielding, and coworkers have performed an extended series of linear stability analysis studies with a variety of constitutive equations to ascertain the conditions under which shear banding occurs in entangled polymeric fluids.[4, 9, 29-39] Specifically, Fielding and Olmsted evaluated the effect of a demixing instability on shear banding, and they demonstrated that shear banding is a mechanical instability in the presence and absence of a nonmonotonic flow curve[9, 29, 33, 36-38]. In a more general study, Moorcroft and Fielding proposed a fluid-universal criteria for the onset of shear banding, namely, the existence of significant stress overshoot in startup of shear flows [34, 35]. The influence of concentration/stress coupling on formation or occurrence of shear banding has also been considered. Cromer *et al.* have demonstrated that this coupling can lead to steady shear banded velocity profiles with monotonic flow curves, albeit in the presence of significant stress overshoot [40].

A recent continuum flow simulation study by Hemingway and Fielding has linked strain banding to edge fracture. Specifically, they observed that existence of moderate edge disturbances could give rise to bulk shear banding [5]. Although, these simulation results are consistent with a few earlier experimental studies cited above, occurrence of shear banding cannot be solely ascribed to edge fracture since shear banding has been observed in a number of experimental studies where the meniscus effect, *i.e*., edge fracture, has been eliminated [41]. The above summary clearly points out that even in absence of concentration/stress coupling and demixing, entangled polymeric fluids can exhibit shear banding under a variety of conditions, namely, monotonic and nonmonotonic flow curves, with and without edge fracture. To this end, what is needed is a molecular picture that paves the way for a full mechanistic understanding of the occurrence of shear banding in entangled polymeric fluids; molecular-level simulations have been increasingly used to gain insight into molecular processing that lead to shear banding.

The first molecular level simulation of shear banding was performed by Cao and Likhtman [42]. They conducted coarse-grained molecular dynamics simulations of short linear monodisperse polymer melts with up to the estimated number of 10 entanglements per chain ($N = 150$; beads)

in a step-strain startup of shear flow using the Langevin and Dissipative particle dynamics thermostat. Transient and steady shear banding was observed after the stress overshoot for monotonic and nonmonotonic flow curves, respectively. Later, Mohageghi and Khomami in a series of papers [7, 43-45] investigated the molecular mechanism leading to shear banding utilizing hi-fidelity Dissipative Particle Dynamics (DPD) simulations in moderately-entangled monodisperse melts up to 26 average number of entanglements per chain in step-strain and finite-strain start-up of bulk shear flows. Their study indicated that shear banding occurs due to inhomogeneous chain segmental orientation and entanglement density of the fluid. The importance of local versus global dynamics of the entanglement network and the influence of deformation ramp rate in startup of shear flow, specifically the appearance of stress overshoot and occurrence of transient and steady shear banding, was also investigated. These comprehensive studies demonstrated that the entanglement network dynamics, *i.e.*, homogenous versus inhomogeneous deformation, is governed by the ratio of chain vorticity excursion time [46, 47] to segmental stretch time. Specifically, they showed that a dimensionless number defined as the ratio of the time for the shear rate to reach its steady value to that of the average vorticity excursion time can be used to quantify the nature of the entanglement network dynamics. If this ratio is greater than unity, then the network disentangles homogenously; hence shear banding is obviated. This indicated that shear banding is not a unique response of entangled polymers [7, 44].

In order to examine the validity of the aforementioned molecular picture as well as its applicability to commercially relevant entangled polymeric fluids, the effect of polydispersity on occurrence of transient and steady shear banding is herein examined via high fidelity DPD simulations [48]. We also examine the effect of molecular weight on the transient and steady-state shear banding phenomenon in startup of shear flow covering a wide range of shear rates.

II. Simulation Methodology

To understand the effects of polydispersity on shear banding in entangled linear polymer melts, we performed equilibrium and nonequilibrium dissipative particle dynamics (DPD) simulations of three mildly polydisperse linear polymer melts using the method introduced by Hoogerbrugge and Koelman [49]. This coarse-grained method integrates Newton's equations of motion for each bead of every polymer chain comprising the melt where the total resultant force exerted on the *i*-th bead is expressed as the sum of the usual DPD force field, $\mathbf{F}_i^{\mathrm{DPD}}$, and two additional forces accounting for the harmonic spring force between adjacent beads, $\mathbf{F}_{ik}^{\mathrm{S}}$, and a bending force between three adjacent beads, $\mathbf{F}_{il}^{bend}$ [45, 48]. The DPD force field is itself comprised of three distinct forces, namely, a conservative pairwise repulsive force, $\mathbf{F}_{ij}^{\mathrm{C}}$, a dissipative force, $\mathbf{F}_{ij}^{\mathrm{D}}$, and a stochastic force, $\mathbf{F}_{ij}^{\mathrm{R}}$, each acting in direction $\hat{\mathbf{e}}_{\mathrm{ij}} = \mathbf{r}_{ij}/r_{ij}$, which is the unit vector quantifying the shortest path between the respective particles. The dissipative and random

forces represent the viscous forces acting within the nonequilibrium melt [50]. In equation form, the DPD simulation framework is described by the following forces acting on each particle $\mathbf{F}_i^{\text{total}}$.

$$\mathbf{F}_i^{\text{DPD}} = \sum_{j \neq i} \left(\mathbf{F}_{ij}^{\text{C}} + \mathbf{F}_{ij}^{\text{D}} + \mathbf{F}_{ij}^{\text{R}}\right), \quad (1)$$

$$\mathbf{F}_{ij}^{\text{C}} = a_{ij}\left(1 - {}^{r_{ij}}\!/_{r_c}\right)\hat{\mathbf{e}}_{ij}, \quad (2)$$

$$\mathbf{F}_{ij}^{\text{D}} = -\gamma_D \omega^D(r_{ij})[(\Delta\mathbf{v}_{ij}).\hat{\mathbf{e}}_{\text{ij}}]\,\hat{\mathbf{e}}_{ij}, \quad (3)$$

$$\mathbf{F}_{ij}^{\text{R}} = \sigma\omega^R(r_{ij})\zeta\,\hat{\mathbf{e}}_{ij}, \quad (4)$$

$$\mathbf{F}_i^{\text{total}} = \mathbf{F}_i^{\text{DPD}} + \mathbf{F}_{ik}^{\text{S}} + \mathbf{F}_{il}^{bend}, \quad (5)$$

$$\mathbf{F}_{ik}^{\text{S}} = k_s(b_{eq} - b_{ik}), \quad \text{for } k = i \pm 1 \quad (6)$$

$$\mathbf{F}_{il}^{bend} = -k_{bend}\sin\theta, \quad \text{for } l = i \pm 2 \quad (7)$$

In these equations, m, r_c, and k_BT are the base units for mass, length, and energy, respectively. This allows other parameters to be expressed in DPD units, such as time $\tau = (mr_c^2/k_BT)^{0.5}$. In Eq. (2), $a_{ij} = 200$ is the repulsion constant acting between particles i and j. This force linearly declines by the ratio (r_{ij}/r_c) (the distance between particles and the cutoff distance), where $r_c = 1$ in DPD units. The dissipative force of Eq. (3) is expressed in terms of the velocity differences of the particles, $(\Delta\mathbf{v}_{ij} = \mathbf{v}_i - \mathbf{v}_j)$, a friction coefficient, $\gamma_D = 4.5$, and a weighting factor that is related to the weighting factor of the stochastic force as $\omega^D = (\omega^R)^2$. Finally, the stochastic (random) force, Eq. (4), is modelled using the random variable ζ of a standard normal distribution, where the weighting factor is defined as $\omega^R = \left(1 - {}^{r_{ij}}\!/_{r_c}\right)$. Moreover, the amplitude parameter, σ, is also linked to the dissipation friction coefficient, γ_D, through the fluctuation-dissipation theorem as $\sigma^2 = 2\gamma_D k_BT$ [49-52]. The intramolecular force parameters of the harmonic bond potential appearing in Eqs. (6) and (7) are the spring constant, $k_s = 400$, equilibrium bond length, $b_{eq} = 0.95$, and the bending constant of our stiffening bend-angle potential , $k_{bend} = 2.0$ [7, 43-45]. The application of soft bending potential is to obtain the correct properties of the polymer chains in a specific course-graining level. It is evident that in highly course-grained models, the bending potential is featureless. To satisfy the topological constraints in the simulations of entangled melts, chain crossing has been prevented by tuning the conservative force developed by Nikunen *et al.* [53] using a computationally efficient strategy. These simulations are similar to those of recent studies involving a coarse-grained model for linear polyethylene melts [48] and are strictly exact with the coarse-grained monodisperse DPD

model used recently by Mohagheghi and Khomami to study shear banding in linear monodisperse melts [7, 43, 44].

The equilibrium and nonequilibrium DPD simulations were performed in the canonical NVT ensemble with a reduced particle density of $\rho = 1$ and reduced temperature $k_BT = 1$ (all in DPD units). The LAMMPS platform was used to integrate the Newton's equations of motion using the velocity-Verlet algorithm with a reduced time step of $\Delta t = 0.012\tau$, along with the Lagrangian rhomboid periodic boundary conditions [54]. The components of the stress tensor were calculated using the Irving-Kirkwood formula [55] implemented within LAMMPS. More details regarding the DPD model for entangled polymers can be found elsewhere [7, 45].

In a recent article [48], we compared DPD simulation data with those derived from the classical equilibrium and nonequilibrium molecular dynamics simulations of entangled polyethylene melts and extracted direct scaling factors for length, time, and viscosity to calculate rheological and structural properties in physical units from DPD simulations that could be compared directly with experimental data (specifically, for entangled polyethylene melts). This allowed us to determine the optimum values of the DPD parameters for polyethylene melts, and a general guideline for establishing optimum parameters for other similar flexible entangled polymer melts. In this article, however, we assume the same DPD parameters as used previously by Mohagheghi and Khomami to study shear banding in linear monodisperse melts [7, 43, 44] in order to facilitate comparisons with that work.

We examined shear banding in three entangled polydisperse polymer melts with polydispersity indices larger than unity ($PDI = {N_w}/{N_n} > 1$) undergoing startup shear flow at intermediate and high shear rates in the dimensionless Weissenberg number ($Wi \equiv \dot{\gamma}\tau_{d_{eq}}$, where $\tau_{d_{eq}}$ is the disengagement time of the melt at equilibrium) range $10 < Wi < 5000$. Note that the longest decorrelation time of the melt, τ_d, decreases as Wi increases, and is only equivalent to the disengagement time ($\tau_{d_{eq}}$) at low deformation rates ($Wi \leq 1$) [46, 56-58]. As discussed above, each particle is assigned a unit mass, $m_{bead} = 1$, at the DPD scale. Thus the mass-average bead number per chain (N_w) and number-average bead number per chain (N_n) are calculated as $N_w = m_{bead}{\sum_i (n_i {N_{c,i}}^2)}/{\sum_i (n_i N_{c,i})}$ and $N_n = m_{bead}{\sum_i (n_i N_{c,i})}/{\sum_i n_i}$, where n_i denotes the number of molecules with $N_{c,i}$ beads and the total number of molecules is $\sum_i n_i$. Two of the melts were defined with mean bead number of $N_n = 250$ and were narrowly dispersed with $PDI = 1.025, 1.05$, such that the constituent chains possessed bead numbers within the range of $N_{c,i} \in [140, 360]$ and $N_{c,i} \in [120, 500]$, respectively. The third melt was defined by $N_n = 400$, $PDI = 1.025$, with the individual chains ranging in bead number over the range $N_{c,i} \in [260, 540]$. All melts consisted of chain lengths ranging from the low to high value in increments of ΔN_c

$= 20$, which was chosen to be larger than the average number of beads per kink segment ($N_n/\langle \boldsymbol{Z_{keq}} \rangle \approx 15$ for all melts) at equilibrium. The number of entanglements per chain, Z_k, was extracted based on topological analysis using the Z1-code [59-62] by Kröger; this ensured that the polydisperse systems covered a wide range of chain entanglements. Note that ensemble averaged number of kinks, $\langle \boldsymbol{Z_{keq}} \rangle$, is approximately twice the value of the number of theoretical entanglements , Z_{coil}, (based on the tube model at equilibrium), $\langle \boldsymbol{Z_{keq}} \rangle \approx 2Z_{coil} \equiv 2\langle L_{pp} \rangle^2 / \langle R^2 \rangle$, where the numerator is the ensemble average of the primitive chain path squared and the denominator is the ensemble average of the magnitude of the chain end-to-end vector. Herein, we use $\langle Z_k \rangle$ as an estimate of the entanglement network since we are not certain that the theoretical relationship for Z_{coil} is valid far from equilibrium. These three melts allowed us to examine the effects of both polydispersity at constant chain length and molecular weight at constant PDI on the shear banding phenomenon. Figure 1 displays the distribution function of chain length for all the melts. Note that the $N_n = 250$, $PDI = 1.025$ and $N_n = 400$, $PDI = 1.025$ melts possess Gaussian distributions, whereas the $N_n = 250$, $PDI = 1.05$ melt displays a log-normal distribution.

The first melt (N250/1.025) consisted of 960 chains within a cell of dimensions $98.6 \times 49 \times 49\, r_c^3$ (corresponding to the flow, x, shear, y, and vorticity, z, directions), whereas the second melt (N250/1.05) contained 1249 chains in a simulation box with dimensions of $108 \times 54 \times 54\, r_c^3$. The third melt (N400/1.025) was constituted of 720 chains in a cell with dimensions of $198 \times 38 \times 38\, r_c^3$. The box sizes were chosen to be large compared to the equilibrium average radius of gyration of the chains to prevent individual chain periodicity interactions under flow conditions where the chains stretch and align in the flow (x) direction. To ensure the homogeneity of the polydisperse melt with respect to chains of differing length, the bead number distribution of chains, $P(N_{c,i})$, was inspected for the N250/1.05 melt within several layered sub-cells within the simulation box over a wide range of Wi. The layer distributions were practically identical with those of the overall simulation cell, such as those depicted in Figure 1.

FIGURE1 Here (Fig1)

Figure 1. The Probability distribution function of chain length in each of the polydisperse melts. The inset shows the number of chains of each polymer length.

We calculated the longest relaxation time (τ_d) by fitting an exponential function to the autocorrelation function of the normalized end-to-end unit vector, $u = \mathbf{R}/\|\mathbf{R}\|$: $AC(t) =$

$\langle u_i(t_o) \cdot u_i(t_o + t) \rangle = \sum_{i=1}^{n} a_i e^{-t/\tau_i}$, using expressions with both two and three exponential terms; the results were statistically equivalent in all cases. Similarly, the longest relaxation time under flow (*i.e.*, the decorrelation time, τ_d, which is equivalent to the disengagement time under quiescent conditions [63]) and chain tumbling period (τ_{rot}) were estimated by the addition of a cosine term to the normalized end-to-end autocorrelation function, $AC(t) = ae^{-t/\tau_d} cos(\frac{2\pi t}{\tau_{rot}})$ [63]. This function adequately captures the damped periodic character of the autocorrelation function associated with the tumbling dynamics of the individual molecular chains [56, 57, 63].

III. Results and discussion

Some key physical properties of the polymer liquids under quiescent conditions as derived from the simulation data are summarized in

Table 1. The ensemble average of squared end-to-end distance, $\langle R_{eq}^2 \rangle^{1/2}$, average number of kinks, $\langle Z_{k_{eq}} \rangle$, as well as the theoretical entanglement density, $Z_{coil_{eq}} = \langle L_{PP_{eq}} \rangle^2 / \langle R_{eq}^2 \rangle$ for the melts of $N_n = 250$, have been calculated as $28\, r_c$, 16, and 9.2, respectively. Similarly, the same parameters for the melt $N_n = 400$ are determined as $\langle R_{eq}^2 \rangle^{1/2} = 35.7\, r_c$, $\langle Z_{k_{eq}} \rangle = 25$, and $Z_{coil_{eq}} = 14$. The number of kinks per chain, $\langle Z_k \rangle$, $Z_{coil_{eq}}$, and the length of primitive path, $\langle L_{PP} \rangle$, were evaluated using Z1-code [59-62]. Note that the above parameters for the first two melts sharing $N_n = 250$ are invariant of polydispersity index. However, the disengagement time, $\tau_{d_{eq}}$, strongly varies between the cases with PDI of 1.025 and 1.05. The disengagement time was calculated as $\tau_{d_{eq}} = 1.3 \times 10^6$, and $\tau_{d_{eq}} = 2.33 \times 10^6$ in reduced time units for the N250 liquids with polydispersity index of 1.025 and 1.05, respectively, and similarly as $\tau_{d_{eq}} = 6.1 \times 10^6$ for the N400 melt. The Rouse and entanglement times were then calculated from the theoretical expressions $\tau_R = \tau_{d_{eq}} / 3Z_{coil_{eq}}$ and $\tau_e = \tau_R \pi^3 / 4Z_{coil_{eq}}^2$ arising from reptation theory at equilibrium conditions[12] . Note that these expressions are based on the assumption that the Rouse and disengagement times scale as $\tau_R \sim N_c^2$ and $\tau_{d_{eq}} \sim N_c^3$, respectively, whereas atomistic simulations of polyethylene melts follow more closely the experimentally observed scaling of $\tau_R \sim N_c^{2.3}$ and $\tau_{d_{eq}} \sim N_c^{3.3}$ [57]. The Mcleish-Likhtman model, incorporating the effect of contour length fluctuations, suggests a correction factor to estimating characteristic times.[64] The Rouse and entanglement relaxation times can be estimated by $\tau_{R,clf} \equiv \tau_{d_{eq}} / 3f(Z)Z$ and $\tau_{e,clf} \equiv \tau_{R,clf} / Z^2$, where $f(Z) = 1 - 3.38/\sqrt{Z} + 4.17/Z - 1.55/Z^{1.5}$is the correction function and Z is effectively $\boldsymbol{Z_{Coil_{eq}}}$. The numerators of correction function are fitting parameters.[65] Table 1 summarizes all

the important parameters. Note that to maintain consistency with prior work, the pertinent parameters in this paper are based on τ_R and τ_e as the Rouse and entanglement relaxation times, respectively.

Table 1. Equilibrium properties for each melt.

N_n/PDI	250/1	250/1.025	250/1.05	400/1	400/1.025
$\tau_{deq}\left(mr_c^2/k_BT\right)^{1/2}$	1.1×10^6	1.3×10^6	2.33×10^6	5.3×10^6	6.1×10^6
τ_R	38,950	47,060	84,420	126,200	145,300
$\tau_{R,clf}$	135,530	166,060	297,880	339,340	398,190
τ_e	3567	4301/3662*	7786/3596*	4426	5738
$\langle R_{eq}^2 \rangle^{1/2}$	$27.8\, r_c$	$28\, r_c$	$28\, r_c$	$35.2\, r_c$	$35.7\, r_c$
$\langle Z_{keq} \rangle$	16	16	16	26	25
$Z_{Coil_{eq}}$	9.4	*9.2*	9.2	14.5	*14*

*These values are based on the mean value of the local τ_e of chains in narrow sections of the overall chain length distribution.

The steady-state behavior of the simulated polydisperse linear melts under shear flow, including viscosity, shear stress, and normal stress differences, were extracted by performing simulations up to $7\tau_d$ (longest relaxation time under flow at any particular Wi). The steady-state shear stress (σ_{xy}) and shear viscosity ($\eta \equiv \sigma_{xy}/\dot{\gamma}$) flow curves of these liquids as functions of Wi are displayed in Figure 2. [Note that σ_{xy} is expressed in this figure using DPD units, so the relative magnitudes of the stress in Figure 2(a) should not be compared directly.] The shear stress of Figure 2(a) for the monodisperse N250 and N400 melts (taken from Ref. [45]) display the same non-monotonic behavior at intermediate Wi as noted previously for atomistic simulations of entangled linear monodisperse polyethylene liquids [46, 47, 56, 57]; *i.e.*, a rapid rise in σ_{xy} in the linear viscoelastic regime up to $Wi \approx 10$, corresponding roughly to $\dot{\gamma} \approx O(\tau_R^{-1})$, where τ_R is the Rouse time, followed by a decrease to a local minimum and then a rapid increase again as $Wi \rightarrow O(100)$, or $\dot{\gamma} \approx \tau_e^{-1}$, where τ_e is the entanglement time of the liquid. [Keep in mind that the N250/1, N250/1.025, N250/1.05, N400/1, and N400/1.025 flow curves are expressed in terms of $Wi \equiv \dot{\gamma}\, \tau_{d_{eq}}$, where $\tau_{d_{eq}}$ is different for each of the five liquids—see Table 1. Then inset of Figure 2(a) shows the stress profiles in terms of shear rate, $\dot{\gamma}$, expressed in DPD units.] Critical values of Wi for each of the three liquids are presented in Table 2.

Table 2. Critical values of Weissenberg number for each melt.

N_n/*PDI*	250/1	250/1.025	250/1.05	400/1	400/1.025
$Wi \equiv \tau_{d_{eq}} \boldsymbol{\tau}_{\boldsymbol{d}_{eq}}^{-1}$	1	1	1	1	1
$Wi \equiv \tau_{d_{eq}} \boldsymbol{\tau}_{\boldsymbol{R}}^{-1}$	28.2	27.6	27.5	43.7	42
$Wi \equiv \tau_{d_{eq}} \boldsymbol{\tau}_{\boldsymbol{e}}^{-1}$	322.8	302/357*	299/669*	1197	1092

*These values are estimated based the mean value of local τ_e of chains in narrow sections of the overall chain length distribution.

Atomistic nonequilibrium molecular dynamics simulations of linear, monodisperse, entangled polyethylene liquids[46, 56, 57] have revealed that the non-monotonic nature of the shear stress profile is caused by the reduction in entanglement density caused by the alignment and stretching of the individual polymer chains under flow—see Figure 2(b), to be discussed below. This reduction in the average number of entanglements per chain degrades the overall tube network, allowing individual chains to undergo semi-periodic tumbling cycles, which effectively relieve elastic tension within the fluid, thereby resulting in a reduction in the shear stress with increasing Wi. Once the tube network has been sufficiently degraded, the individual chains behave similarly to those in a dilute solution, tumbling in periodic cycles of chain compression and extension, effectively scaling shear stress similarly to dilute solution theory [46, 56, 57, 66-69]; ultimately, this leads to the subsequent increase in σ_{xy} beginning at about $\dot{\gamma} \approx \tau_e^{-1}$, which continues to exceedingly high values of Wi.

The effect of polydispersity on the shear stress profile is illustrated in Figure 2(a) for both the N250 and N400 melts. As the *PDI* increases, the magnitude of the decreasing shear stress (*i.e.*, the local maximum followed by a decrease in the shear stress) is lessened with increasing *PDI* until a stress plateau is attained at intermediate shear rates rather than an inverse response, as is commonly observed in experiment of polydisperse linear polymer solutions and melts. Furthermore, the increase in polydispersity index from 1.025 to 1.05 for the N250 fluid has the effect of widening the plateau region of the stress profile. The effect of polydispersity is to broaden the relaxation spectrum of the polymer melt, which effectively implies that chains of differing length, with inherently separate values of $\tau_{d_{eq}}$, experience a range of apparent Wi values at the same shear rate, $\dot{\gamma}$. Hence these chains attain critical shear rates, such as $\dot{\gamma} = \tau_R^{-1}$ and $\dot{\gamma} = \tau_e^{-1}$, at different points on the stress profile. Since these critical points are associated with inception points of dramatic changes in key physical properties, such as entanglement density and the associated onset of tumbling dynamics, the non-monotonic character of the shear stress profile is diluted as it is spread out over a wider range of Wi [45-47, 68]. In other words, by the time shorter chains have attained the critical Weissenberg number to reach the shear stress maximum, longer chains have already attained the Wi at which their minimum is observed,

such that the subsequent increase in shear stress due to the longer chains mitigates the decrease in shear rate induced by the shorter ones.

It is also apparent from Figure 2(a) that increasing the average molecular weight (*i.e.*, average chain length) of a melt requires a greater degree of polydispersity to flatten the profile into a stress plateau at intermediate shear rates. This is possibly because the longer chains possess longer relaxation times and larger average entanglement numbers, which apparently results (see Table 2) in a widening of the effective Wi range over the distribution of chains lengths. (Recall that the nonmonotonic stress profile is most severe in the case where all chains possess the same effective Wi when $PDI = 1$.) Hence the smoothing into the stress plateau is likewise distributed over a wider range of Wi for the polydisperse melts of higher average molecular weight.

The steady-state average number of "kinks" per chain $\langle Z_k \rangle$, is displayed as a function of Wi in Figure 2(b). The monodisperse N250 and N400 melts exhibit qualitatively similar behavior: an approximately constant value in the range $\dot{\gamma} \in [0, \tau_R^{-1}]$, and then a steady decrease for $\dot{\gamma} > \tau_R^{-1}$ in which the entanglement network is practically destroyed at very high $Wi \approx$ O(10,000). The dramatic decline in the average number of kinks per chain begins roughly as $\dot{\gamma} \approx \tau_R^{-1}$, where the individual chains begin to stretch markedly from their quiescent configurations. This results in a net extension and orientation of the tube network along the direction of flow, which relieves some of the associated constraints on the individual chains, thus allowing them more freedom of movement, which ultimately results in the semi-periodic tumbling orbits of the individual chains (as described above) within the extended and enlarged tubes formed by the neighboring chains. Indeed, atomistic simulations of monodisperse, linear polyethylene melts indicate a direct, inverse correlation between chain stretch and entanglement number [47]. As $\dot{\gamma} \rightarrow \tau_R^{-1}$, the entanglement network begins to disintegrate to a degree where the concept of reptation no longer applies, and the inherent dynamics of the melts resemble those of dilute solutions of polymers rather than dense entangled liquids [47, 56, 57].

The effect of polydispersity on the behavior of $\langle Z_k \rangle$ as a function of Wi is also shown in Figure 2(b). In all cases, increasing PDI acts to diminish and broaden the decrease in $\langle Z_k \rangle$, effectively ameliorating the drop in the number of kinks per chain. This broadening is again associated with the range of Wi over which individual chains enter into the shear rate region where $\dot{\gamma} > \tau_R^{-1}$, with longer chains being impacted sooner than shorter ones on the overall flow profile. Increasing the average chain length has the obvious effect of increasing the average number of chain kinks at any Wi. In the flow regime of $\dot{\gamma} \in [\tau_R^{-1}, \tau_e^{-1}]$, the average kink number, $\langle Z_k \rangle$, scales with shear rate as $Wi^{-0.1}$ and $Wi^{-0.08}$ for the N250/1.025 and N250/1.05 melts, respectively, whereas for the melt N400/1.025, $\langle Z_k \rangle$ scaled as $Wi^{-0.12}$. At high shear rates $\dot{\gamma} > \tau_e^{-1}$ (where chain rotation dynamics is the dominant dynamical mechanism), the power-law

exponent decreases to -0.21, -0.28, and -0.21 for the N250/1.025, N250/1.05, and N400/1.025 melts, respectively. Atomistic simulations of linear monodisperse entangled polyethylene melts within $\dot{\gamma} \in [\tau_R^{-1}, \tau_e^{-1}]$ exhibited power-law exponents of -0.27 (-0.32 for $\dot{\gamma} > \tau_e^{-1}$), -0.23 (-0.35 for $\dot{\gamma} > \tau_e^{-1}$), and -0.07 (-0.35 for $\dot{\gamma} > 500$) for melts of $C_{400}H_{802}$, $C_{700}H_{1402}$, and $C_{1000}H_{2002}$, respectively [46, 47, 56, 57]. Hence the DPD data are not unreasonable compared to those of the atomistic liquids.

Figure 2(c) displays the steady-state shear viscosity as a function of Weissenberg number, which exhibits a power-law behavior ($\eta \propto Wi^{\propto}$). The viscosity within the shear rate range $\dot{\gamma} \in [\tau_{d_{eq}}^{-1}, \tau_e^{-1}]$ scales with power-law exponents of -0.97, -0.98, and -0.99 for the N250/1.025, N250/1.05, and N400/1.025 melts, respectively; similarly, the power-law exponents at $\dot{\gamma} > \tau_e^{-1}$ were found to be -0.72, -0.80, and -0.88. These values are reasonably consistent with previous DPD simulations of Mohaghegi and Khomami [7], which reported values of -1.028 and -1.042 for the power-law exponents of monodisperse melts N400 and N250 respectively, as well as the atomistic simulation studies of linear, monodisperse polyethylene melts, such as that of Nafar Sefiddashti *et al.* [57] which found a power-law exponent of -0.88 for a $C_{700}H_{1402}$ melt under steady shear flow within the shear rate range $\dot{\gamma} \in [\tau_{d_{eq}}^{-1}, \tau_e^{-1}]$ and -0.59 for $\dot{\gamma} > \tau_e^{-1}$. Furthermore, the power-law exponent in similar flow regimes for a $C_{400}H_{802}$ linear, monodisperse polyethylene melt were reported as -0.89 and -0.44 [70] and for a $C_{1000}H_{2002}$ melt were -1.1 and -0.79 [46].

From Figure 2(c), it is apparent that the effect of chain length on viscosity is to increase its value regardless of Wi. Of course, this is not a new observation and aligns with all available experimental data[71-73] ; as chain length increases, the entropic elastic effect becomes more pronounced as the longer chains extend and orient with respect to the direction of shear. For the same reason, the effect of polydispersity evident in Figure 2(c) is exactly the same: increasing PDI increases the viscosity since the higher PDI liquid is composed of longer chains on the high end of the chain number distribution (*i.e.*, $N_{c,i} \in [140, 360]$ and $N_{c,i} \in [120, 500]$ for the N250/1.025 and N250/1.05 melts, respectively), and these longer chains have a more pronounced elastic effect on the system response. Again, these observations are in accord with available experimental data [73, 74].

FIGURE 2 Here (Fig2)

Figure 2. (a) Steady-state shear profile ($\sigma_{xy}\ vs.\ Wi$) in DPD units for melts with $N_n = 250$ and 400 with varying PDI. The inset shows the same data expressed in terms of shear rate in DPD units. Data for the monodisperse melts ($PDI = 1$) N250 and N400 were taken from Ref. [45]. (b) the average number of entanglement (Kinks) density, $\langle Z_k \rangle$, versus Wi number. (c) Steady-state viscosity, η, versus Wi number in DPD units. The viscosity shear-thinning exponents for the two shear rate regions of $\dot{\gamma} \in [\tau_{d_{eq}}^{-1},\ \tau_e^{-1}]$ and $\dot{\gamma} > \tau_e^{-1}$ are noted in the plot.

Figure 3(a)-(c) show the steady-state probability distribution functions of the normalized end-to-end distance (with respect to the maximum chain extension based on $N_{c,i}$), $\|\mathbf{R}\|/\mathbf{R}_{max}$, of the three polydisperse melts at several Wi ranging from equilibrium up to $\dot{\gamma} > \tau_e^{-1}$. For all three melts, the normalized end-to-end distance distribution function in the quiescent state is essentially Gaussian. (Note that the N250 melts have almost identical distributions at equilibrium.) Under steady shear flow, the distributions widen and shift toward higher extensions as shear rate increases within the range of $0 < \dot{\gamma} < \tau_R^{-1}$ ($0 < Wi < 28$ for N250 and $0 < Wi < 42$ for N400). At shear rates with a Rouse time-based Weissenberg number larger than $Wi_R \equiv \dot{\gamma}\tau_R > 1$, the distributions flatten and become excessively wide, indicating a very wide distribution of end-to-end chains lengths occupied by the chains at any instant in time. As noted from previous atomistic simulations [45-47, 57, 63], these wide distributions are the ensemble-averaged result of chain tumbling cycles where individual chains rotate and flip in a semi-periodic fashion as induced by the vorticity of the shear field. The frequency and amplitude of these tumbling cycles increase with shear rate, and for $\dot{\gamma} > \tau_e^{-1}$, the distributions shown in Figure 3 can develop bimodal character (although much less distinct than for the corresponding monodisperse melts; data not shown), with a peak at low values of extension (even lower than the quiescent value) associated with the nadir in the cycle where the individual chain ends pass by each other as the end-to-end vector flips sign, and another peak at very high extensions corresponding to individual chains at their maximum values of extension during the apex of the tumbling cycle. As average chain length increases from 250 to 400 beads, the second peak to disappear or be pushed to higher Wi. All of these observations are consistent with prior atomistic simulations of monodisperse linear polyethylene melts [45-47, 58, 63, 69, 70].

Figure 4 presents the temporal evolution of the shear stress of the polydisperse linear polymer melts undergoing startup of shear flow at different Wi as a function of strain. In accordance with reptation theory, the maximum stress of the overshoot occurs at about two strain units ($\gamma_p \cong 2$) for each of the three melts within the range $0 < \dot{\gamma} < \tau_R^{-1}$. As shear rate is increased above τ_R^{-1}, the position of the maximum increases steadily, approaching 5 strain units for $\dot{\gamma} > \tau_e^{-1}$. In all cases, the shear stress attains its steady-state value within about one longest relaxation time (τ_d) at the corresponding shear rate—see the atomistic simulations of Refs. [45-47,

[58, 63, 69, 70] for a discussion of the relationship between τ_d and Wi. At $\dot{\gamma} > \tau_R^{-1}$, the effect of increasing PDI (seen in Figure 4(a)) is to decrease the magnitude of the overshoot significantly and the maximum position slightly to smaller strains. This is consistent with the distribution functions of Figure 3, which indicate that the effect of polydispersity is to increase the breadth of the chain length distributions. Evidently, sharp, tall overshoots are characteristics of melts with very narrow chain length distributions, in which all chains are affected similarly by the imposed flow field. For polydisperse melts, the variations in chain length induce different responses to the changing imposed shear rate under startup conditions. As shown in Figure 4(b), the effect of increasing average chain length is also to decrease the magnitude of the overshoot and shift its position to lower strains; this is once again due to the increase in breadth of the chain-length distributions of the N400 melt over the N250 melt presented in Figure 3.

FIGURE3 Here (Fig3)

Figure 3. Probability distribution of chain end-to-end length normalized by chain maximum extension (a). Panel (b) illustrates the effect of polydispersity on the chain distributions, expressed in terms of the magnitude of the end-to-end vector in DPD units. Panel (c) illustrates the effect of average chain length on the distributions.

FIGURE4 Here (Fig4)

Figure 4. Startup shear stress evolution as a function of shear strain. Panel (a) illustrates the effect of polydispersity for the N250 melt, whereas Panel (b) shows the impact of average chain length.

Shear banding in polydisperse melts

Prior theoretical studies have attributed strain localization to the shear stress overshoot [34, 35]; *i.e.*, the elastic and viscous instabilities that induce shear banding are associated with overshoot in a finite step-strain or startup of shear flow. Shear banding, which has been shown to initiate just after the occurrence of the overshoot is the result of elastic-like instabilities at the shear rates of $\dot{\gamma} \gg \tau_{d_{eq}}^{-1}$. This has been validated by molecular-level simulations of monodisperse polymeric fluids [7, 42-44]. The introduction of polydispersity makes the nonlinear dynamics of

polymers more complex. As discussed above, the level of nominal entanglement density and polydispersity have a significant effect on the shape of the constitutive stress profile and the occurrence of expected instabilities. In this section, the macroscopic flow characteristics of polydisperse melts are presented and discussed in detail. We track the evolution of the system velocity profile in simulations of startup of shear flow at various Wi spanning shear rate ranges $\dot{\gamma} > \tau_{d_{eq}}^{-1}$. The simulation box was subdivided into 20 layers along the shear gradient direction (y-axis), and the velocity profiles were extracted by temporal averaging over time increments of 0.1 τ_d. Both N250 melts displayed monotonic shear stress flow curves in this flow regime—see Figure 2(a). Simulation results revealed the existence of transient shear banding in both cases, as shown below, which ultimately decayed to a linear profile spanning the simulation cell once steady state had been attained.

Figure 5(a) illustrates the temporal evolution of shear bands in the N250/1.025 melt at $Wi = 30$, which persist up to $t = (6\text{-}7)\ \tau_d$, where τ_d is the longest relaxation (decorrelation) time of the melt at the stated Wi. The main plot displays the shear stress versus normalized time, with a tall overshoot appearing close to the theoretical strain of 2 units (at $t = 0.15\tau_d$), followed by a slow decay to the steady-state value after about 21 strain units, corresponding to about $t = \tau_d$. At the time when the maximum occurs, the velocity profile across the simulation cell is linear, and the distributions of the chains are as would be expected from classical rheological theory: a residual Gaussian shape that is stretching toward higher chain extensions, with all three chain-length regimes (orange curve:$N_{c,i} \in [140, 220]$, green curve: $N_{c,i} \in [240, 260]$, and red curve: $N_{c,i} \in [280, 360]$) showing essentially identical behavior. Once past the maximum, however, by $t = 0.4\tau_d$ ($\gamma \approx 6$), an evident transient shear band has appeared in the simulation cell, as indicated by a scaled velocity profile (V/V_{max}) that manifests two linear regions of different slope (shear rate) spanning the scaled simulation cell dimension in the y-direction (Y/H). At the same time, the distributions, although still identical, have significantly broadened, indicating the onset of chain tumbling and entanglement disintegration. Although the shear stress appears to have attained steady state by $t = \tau_d$ ($\gamma \approx 21$), the transient shear bands are still readily observed, and the distributions of chain length have broadened significantly and become individually distinct, as indicated in Figure 3above. It is not until $t = (6\text{-}7)\ \tau_d$ ($\gamma \approx 100$) when the shear bands merge into a single linear velocity profile spanning the entire simulation cell and the chain length distributions settle into their steady-state flow curves, exhibited in Figure 3. So although the shear stress attains its steady-state value within about one τ_d, it is not until much later that other critical physical characteristics of the polydisperse melt settle into a steady state and the short-lived instabilities giving rise to the distinct shear bands disappear. At later times, it is still possible that random thermal perturbations or edge effects might disturb the linear velocity profile for short periods of time.

FIGURE 5(a) Here (Fig5(a))

FIGURE 5(b) Here (Fig5(b))

Figure 5. The temporal evolution of shear stress vs. normalized time for melt N250/1.025 undergoing startup shear flow at (a) $Wi = 30$ and (b) $Wi = 60$. Figures include the evolution of the velocity profile and the probability distribution function of the end-to-end vector magnitude normalized by maximum chain length. Distributions are color-coded based on chain length as follows: orange for $N_{c,i} \in [140, 220]$, green for $N_{c,i} \in [240, 260]$, and red for $N_{c,i} \in [280, 360]$.

The effect of increasing the shear rate on transient shear banding during startup flows is illustrated in

Figure 5(b) for the N250/1.025 melt at $Wi = 60$. In this case, the height of the stress overshoot has grown although its width has narrowed appreciably. The maximum occurs at $\gamma = 3$ (although still occurring at $t = 0.15\tau_d$; recall that τ_d decreases with increasing Wi [56-58]), where the velocity profile is observed to be linear. The stress attains steady state at approximately $t = \tau_d$, similarly to the case of startup at $Wi = 30$—see

Figure 5(a). Shear banding is initiated after the stress passes through its maximum and remains present until well after the shear stress has attained its steady-state value, up until dying out at roughly $t = (5\text{-}6)\ \tau_d$ ($\gamma \approx 115$). The distributions of the various chain-length regimes are very similar to those observed in the $Wi = 30$ simulation. Hence the primary effect of increasing the Wi of the startup flow is to shift the position of the maximum beyond the theoretical prediction of $\gamma = 2$ and to increase the magnitude of the overshoot while narrowing its width. The dynamics of the transient shear-banding phenomenon, however, remain largely unchanged.

The effect of polydispersity on the startup shear-banding dynamics at constant shear rate can be examined by comparing the N250/1.025 melt of

Figure 5(b) with the N250/1.05 melt of Figure 6(a) at $Wi \approx 60$. The first significant difference is that the N250/1.05 melt maintains the theoretical position of the maximum at $\gamma = 2$ at a far higher Wi than the N250/1.025 melt. Furthermore, any shear banding present in the N250/1.05 melt lags behind (in time) slightly that of the less polydisperse melt, and the velocity profiles in

the shear bands are much less distinct; indeed, they are almost linear and cannot readily be identified as transient shear banding structures. At higher Wi, most dynamical characteristics of the N250/1.05 melt are very similar to those of the less polydisperse N250/1.025 melt, as discussed above: transient shear bands form for times past the occurrence of the maximum (at $t = 0.2\tau_d$), the shear stress attains steady state at about $t = \tau_d$, and the shear bands decay after about $t = 6\tau_d$. Both melts experience a decrease in the lifetime of the instabilities at flow rates of $Wi > 100$. The N250/1.05 melt shows strain localization within range of $Wi \in [52,\ 500]$ over a time period of $t \in [0.4, 7)\ \tau_d$. Further increase in flow rate to $Wi > 500$ results in short-lived instabilities similarly to those which occur N250/1.025 melt, to the extent that for a very high shear rate of $Wi = 862$, a linear velocity profile is established as early as $t = 2\tau_d$.

FIGURE 6(a) Here (Fig6(a))

FIGURE 6(b) Here (Fig6(b))

FIGURE 6(c) Here (Fig6(c))

Figure 6. The temporal evolution of shear stress vs. normalized time for the N250/1.05 melt undergoing startup of shear flow at (a) $Wi = 52$, (b) $Wi = 86$, and (c) $Wi = 216$. Figures include the evolution of the velocity profile and the probability distribution functions of the end-to-end vector magnitude normalized by maximum chain length. Distributions are color-coded based on chain length as follows: yellow for $N_{c,i} \in [120, 220]$, green for $N_{c,i} \in [240, 260]$, red for $N_{c,i} \in [280, 360]$, and red for $N_{c,i} \in [380, 500]$.

The development of shear banding relies on the topological relaxation of macromolecular chain and chain segments within an entangled network. Considering the distinction among the dynamics of components, we have investigated the response of different chains to the imposed flow rate.

Figure 5and 6 depict the instantaneous probability distributions of the normalized end-to-end distance and the corresponding velocity profiles at different times ranging from $t = 0.15\tau_d$, $0.4\tau_d$, $1\tau_d$, and at the time a linear profile is fully developed $t = (5\text{-}7)\ \tau_d$. To this end, individual chains of the N250/1.025 melt have been divided into three, and for the N250/1.05 melt, four ensembles, based on chain length, $N_{c,i}$. As observed in

Figure 5 and 6, chain normalized end-to-end vector distributions are almost identical in terms of their stretching behavior at the overshoot time, and later at the onset of shear banding, $t = 0.4\,\tau_d$. However, as the flow develops, the high population of short chains ($N_{c,i} \leq 220$) retreat to a less-stretched distribution with a wide peak and a long tail toward stretched configurations. We can attribute this behavior to the low level of entanglements of this portion of the fluid and its fast dynamics. On the contrary, longer chains ($N_{c,i} \geq 240$) show a semi-flat distribution with a higher peak for the stretched configuration at $t = \tau_d$. Later, as shear banding disappears ($t = 5\text{-}7\ \tau_d$), the chains retract in favor of more coiled configurations, and hence more entanglements (see Figure 8 below) resulting in a semi-flat distribution with a higher peak around the equilibrium peak position.

The different dynamics of the chains are due to the wide spectrum of relaxation timescales of the disparate chains within the polydisperse melts. As discussed earlier, by increasing the flow rate to $\dot{\gamma} \geq \tau_R^{-1}$, chains experience greater tube stretching and more frequent rotation cycles. Unlike monodisperse melts, components in a multicomponent fluid undergo different flow regimes based on their characteristic timescales. Although, separate chains follow different dynamics, the more populated chains dominate the system dynamics, especially in regard to chain tumbling mechanism. In general, the simulations indicate that polydisperse melts exhibit an inhomogeneous state while the imposed shear rate is $\dot{\gamma} \geq \tau_{R_{chains}}^{-1}$ for a substantial portion of the chains. The result of any further increase in deformation rate to $\dot{\gamma} \geq \tau_e^{-1}$, where the stress profile again becomes an increasing function of strain over the plateau, is a faster reorientation and stretching dynamics. Thus, a quasi-periodic vorticity excursion dominates the dynamical behavior, which boosts the mixing effect and shortens the lifetime of the shear bands down to 2 τ_d (not shown in the figures). The shear rates $Wi = 30$ and $Wi = 60$ of the N250/1.025 melt (

Figure 5(a),(b)) satisfy the condition is $\dot{\gamma} \geq \tau_{R_{chains}}^{-1}$ and consequently shear-banded structures are observed. At $Wi = 60$, the condition holds as $\tau_{R_{280\sim360}}^{-1} < \tau_{R_{240\sim260}}^{-1} < \tau_{R_{140\sim220}}^{-1} \leq \dot{\gamma}_{flow} < \tau_e^{-1}$ (approximately $26 < 32 < 43 \leq Wi < 318$, respectively). Interestingly,

Figure 5 exhibits a two-layered velocity profile for $Wi = 30$ and a four-layered velocity profile at $Wi = 60$ at $t = \tau_d$. This can be explained by the flat distribution of chains representing more frequent rotation/retraction cycles at $Wi = 60$ relative to $Wi = 30$. Similarly, at $Wi = 216$ for the N250/1.05 melt shown in Figure 6(c), the shear rate satisfies the condition $\tau_{R_{240\sim260}}^{-1} < \tau_{R_{120\sim180}}^{-1} \leq \dot{\gamma}_{flow}$ (approximately $65 < 124 \leq Wi$), and the banded structure appears within the time period of $t = 0.4\text{-}7\tau_d$. At the shear rate of $Wi = 52$, shown in Figure 6(a), only a few perturbations can be observed. Increasing the shear rate to $Wi = 86$, the perturbations grow and two layers with different local strain rates develop. The large range of relaxation times of the chains of various lengths apparently leads to an unstable interface between the bands due to the

different dynamics of the individual chains despite the overall network effect of the surrounding macromolecules. The velocity profiles embedded in

Figure 5 and 6 exhibit adjacent fast and slow bands separated by distinct interfaces. The width of the bands in the simulation cell is a strong function of shear rate. At low shear rates, only two equal bands were observed, while under stronger flow conditions (mostly for $\dot{\gamma} \geq \dot{\tau}_e^{-1}$), the fast region is dominant within the cell.

Figure 7 illustrates the effect of average molecular weight (*i.e.*, average chain length) on the temporal stress evolution of the more entangled N400/1.025 melt undergoing startup of shear at a deformation rate of $Wi = 100$. Similarly, to the N250 melts, the perturbations in the velocity profile initiate after the stress overshoot (at $\gamma \cong 2$) and continue to develop into fully structured bands at $t \approx \tau_d$. Unlike the less entangled melts, however, we observe a long-lasting (*i.e.*, a steady state) shear banding phenomenon. Moreover, the distributions of the different chain ensembles indicate similar dynamics of the chains throughout the evolution of the flow. The net result is that the longer chain system, although still polydisperse, behaves more like a monodisperse melt than a shorter chain liquid of the same PDI. [Note that the N400/1.025 melt displays a nonmonotonic stress profile—see Figure 2(a).]

FIGURE 7 Here (Fig7)

Figure 7. The evolution of shear stress vs. normalized time for steady shear flow at $Wi = 100$ of the N400/1.025 melt, including the evolution of the velocity profile and the probability distribution functions of the end-to-end vector magnitude by normalized by maximum chain length. Distributions are color-coded based on chain length as follows: yellow for $N_{c,i} \in [260, 360]$, green for $N_{c,i} \in [380, 420]$, and red for $N_{c,i} \in [440, 540]$.

Previous studies linked the cause of shear banding to the local orientation and disentanglement of the constituent polymer chains [26, 43, 44]. Therefore, we have extracted the chain entanglement densities and primitive path lengths for a subset of the simulations discussed above using the Z1-Code. Figure 8 illustrates the evolution of the chain normalized entanglement density distribution, $Z_n \equiv {Z_{k,i}}/{\langle Z_{k,i_{eq}} \rangle}$ where $Z_{k,i}$ is per chain entanglement normalized by $\langle Z_{k,i_{eq}} \rangle$ as the average number of kinks for chain $N_{c,i}$ at equilibrium, of two distinct shear rate zones, one associated with a relatively high shear rate (fast band) and the other with a low shear rate (slow

band) for the N250/1.05 melt at $Wi = 216$. It is evident that the linear velocity profiles only exist at the times ($t = 0.15\tau_d,\ 7\tau_d$), where the layers have similar entanglement distributions. The fast layer starts to disentangle with higher rate as early as $t = 0.4\tau_d$, which causes a strain localization and chain length demixing phenomenon to develop and thereby induce a flow composed of two distinct shear rate regions. As the slow band experiences a lower imposed shear rate, there is lower driving force to disentangle the chains within this flow regime relative to the high shear rate zone. As flow continues, however, it is likely that the rotational tumbling cycles of extension and retraction dynamics lead an unstable interface which induces a remixing of the chains. Eventually, the difference between the entanglement distributions declines and flow continues with a linear velocity profile spanning the simulation cell possessing a single shear rate.

FIGURE 8 Here (Fig8)

Figure 8. The evolution of the normalized entanglement density distribution, $Z_n \equiv {Z_{k,i}}/{\langle Z_{k,i_{eq}} \rangle}$, for the N250/1.05 melt at $Wi = 216$ within the high shear rate layer (fast band) and low shear rate layer (slow band) during the course of startup shear flow at various critical values of elapsed time: (a) linear velocity profile at the overshoot time, $t = 0.15\tau_d$; (b) perturbation in velocity profile is observed at $t = 0.4\tau_d$; (c) fully developed shear-banded structure is observed at $t = \tau_d$; (d) transient shear banding decays and linear velocity profile reemerges at $t = 7\tau_d$.

To characterize the flow in different layers, **Error! Reference source not found.** presents the evolution of the shear stress and the first normal stress differences ($N_1 = \sigma_{xx} - \sigma_{yy}$) for two adjacent shear bands with different local shear rates for the N250/1.05 melt undergoing startup flow at $Wi = 215$. The shear stress evolution is essentially identical in both the fast and slow bands, whereas the band exhibits a greater N_1 for times greater than the instant of the overshoot maximum. The N_1 maximum ($t \approx 0.3\tau_d$) occurs later than the shear stress maximum ($t = 0.15\tau_d$); indeed, the maximum in the first normal stress difference occurs at approximately the same instant in which the shear bands first appear—see Figure 6(c)—indicating that the elastic stress is essentially responsible for the development of the shear instability. Both σ_{xy} and N_1 attain approximate steady-state values at $t = \tau_d$, and the difference between the N_1 values at this time is roughly 25%. As the bands gradually decay for $t > 5\tau_d$, the N_1 layer values converge to a common value as the linear velocity profile emerges. Consequently, it appears that the transient shear banding initiated in this system is a direct result of an elastic instability, rather than a viscous one.

Data show different characteristics of the end-to-end distance for chains within the fast and slow bands. At the stress overshoot time, identical chain end-to-end distance distribution profiles

are observed; however, as perturbations increase, the end-to-end distance of chains in a fast band obtain a broad distribution with a long tail, whereas chains located within a slow region obtain a single peak distribution with a shorter tail. The differences of the distributions remains as long as spatial strain localization is maintained. As flow attains a spatially homogenous state, the distributions of end-to-end distance converge. Also, our results (not shown here) indicate that the end-to-end distances of chains within low shear rate bands may not experience an elevated overshoot, whereas chains within fast bands always experience a notable overshoot in transient shear flow. The overshoot of the ensemble mean end-to-end distance coincided with the tail of transient stress relaxation. These observations are consistent with the argument of initiation of instabilities based on N_1 results discussed above.

FIGURE 9 Here (Fig9)

Figure 9. Shear stress and first normal stress differences for steady shear flow at $Wi = 215$ of the N250/1.05 melt within the fast and slow bands.

Figure 10 displays the average number of kinks per chain located in different layers along the velocity gradient direction scaled as Y/H at $t = 0.4\tau_d$ (the approximate time of shear band initiation in each case) for the three melts at various Wi. Notably, in comparison with the slow bands, the fast bands obtain a lower average number of kinks per chain. Moreover, to measure the alignment of the chains the orientation angle has been estimated by measuring the angle between the flow direction and the largest eigenvalue corresponding to the eigenvector of the order tensor, $\boldsymbol{S} \equiv \langle 3\hat{\mathbf{u}}\hat{\mathbf{u}} - \mathbf{I}\rangle/2$, where $\hat{\mathrm{u}}$ denotes the unit vector of the chain primitive path (PP) segments, as computed via the Z1 code. Figure 11 shows the probability distribution of the orientation angle corresponding to PP segments in adjacent fast and slow bands of the N250/1.05 melt undergoing startup shear flow at $Wi = 215$. (This result is typical of the other melts at various Wi as well.) The data indicates that segments in the fast bands obtain a more narrow distribution centered at a lower orientation angle, whereas segments in the slow zones obtain a relatively wide distribution at moderately higher values of the orientation angle, θ_{xy}. This observation is consistent with the previously proposed molecular mechanism for the onset and development of shear banding instabilities.

FIGURE 10 Here (Fig10)

Figure 10. Mean kink number per chain placed in each band at $t = 0.4\tau_d$. The tall peaks in each profile indicate the normalized locations of the slow bands with greater kink density.

FIGURE 11 Here (Fig11)

Figure 11. The probability distribution function of the orientation angle (with respect to the flow direction) of chain primitive path segments in the x-y plane for the fast and slow layers at $t = \tau_d$ of $Wi = 215$ of the N250/1.05 melt.

As discussed in Ref. [43], based on a hydrodynamic interfacial stability analysis, three factors influence the interfacial stability in stratified shear-banded flow; namely depth ratio, $\varepsilon = \left[{d_{slow}}/{d_{fast}}\right] \leq 1$, band elasticity ratio, $E = \left[{N_1^{fast}}/{N_1^{slow}}\right] \cong \mathcal{O}(1)$, and viscosity ratio, $R = \left[{\eta_{slow}}/{\eta_{fast}}\right] > 6$. The simulation data presented above is consistent with these quantifications. In particular, the $N_n = 250$ melts have, $R < 6$, whereas the $N_n = 400$ melt has a viscosity ratio estimated to be $R \approx 17$, far beyond the critical limit where steady-state shear banding could manifest. Hence the observations of transient and steady-state strain bands as described above are entirely consistent with the stability analysis.

In addition, the shear stress overshoot under startup flow conditions hints at the possibility of stress localization as a mechanical instability, in which case, based on theoretical analysis, overall stress can be reduced by the formation of higher strain rate zones. Comparing the onset of shear banding in polydisperse systems with previous studies [43, 44] of monodisperse systems, we can suggest a critical measure in formation of inhomogeneity. As observed in the simulated polymer melts, strain localization is expected as long as $(\sigma_{xy}^{Overshoot} - \sigma_{xy}^{Steady})/\sigma_{xy}^{Steady} > 1$. The former expression is a measure of both orientation and affine stretching, whereas the same expression for N_1 mostly represents the stretching of the chains. Data above indicate that the precise location in time of the first normal stress difference is a strong predictor of the onset of shear band formation.

Some experiments and analysis using the Roly-Polie model predict shear banding in a specific gap size or geometry curvature and perturbation levels [34, 37]; however, our simulations indicate

the possibility of shear banding in a simple step-strain Couette flow. We examined the bead number distribution in fast and slow zones during the flow, but the results do not indicate any phase separation or chain migration (although, chain migration in an entangled melt is a relatively slow process).

IV. Conclusions

The effects of polydispersity, chain length and in turn entanglement density on the development of shear banding instabilities in three well-entangled polydisperse linear polymer melts undergoing steady shear flow and startup of shear flow were investigated over a wide range of shear rates via dissipative particle dynamics simulations. It was demonstrated that the degree of polydispersity is correlated with the decline in nonmonotonicity of the shear stress profile due to a wide spectrum of relaxation timescales inherent to polydisperse melts. The presence of longer molecules in the chain length distribution also broadened the stress plateau, an effect that increased with increasing polydispersity index. Evidently, melts possessing longer mean chain lengths (N_n) require greater polydispersity to produce a monotonic stress plateau profile. Transient shear banding was observed in shorter chain melts undergoing startup of shear flow in which instabilities arose after the appearance of a stress overshoot, almost concurrently with the overshoot in the time evolution of the first normal stress difference. These instabilities eventually decayed, but only long after the stresses had attained their steady-state values. The longer chain melt exhibited a shear band structure that remained indefinitely, long after the stresses had attained steady state. The development of strain localization in the startup of shear simulations was realized for shear rates higher than inverse of rouse relaxation time scale, $\tau_{R_{chains}}^{-1} \leq \dot{\gamma}_{imposed}$.

V. Acknowledgements

Computational resources for this project were provided by the National Institute for Computational Sciences and the ORNL Joint Institute for Computational Sciences. Financial support was provided by NSF under CBET-1602890. This work also used the Extreme Science and Engineering Discovery Environment, which is supported by NSF (ACI-1548562) using Bridges (TG-CTS150054).

VI. Conflicts of interest

The authors declare that there are no conflicts to declare.

References

1. M. M. Denn, *Annual Review of Fluid Mechanics*, 2001, **33**, 265-287.
2. T. Divoux, M. A. Fardin, S. Manneville and S. Lerouge, *Annual Review of Fluid Mechanics*, 2016, **48**, 81-103.
3. C. M. Schroeder, H. P. Babcock, E. S. Shaqfeh and S. Chu, *Science*, 2003, **301**, 1515-1519.
4. S. M. Fielding, *Soft Matter*, 2007, **3**, 1262-1279.
5. E. J. Hemingway and S. M. Fielding, *Physical Review Letters*, 2018, **120**, 138002.
6. S.-Q. Wang, *Macromolecular Chemistry and Physics*, 2019, **220**, 1800327.
7. M. Mohagheghi and B. Khomami, *Journal of Rheology*, 2016, **60**, 861-872.
8. M. Johnson Jr and D. Segalman, *Journal of Non-Newtonian Fluid Mechanics*, 1977, **2**, 255-270.
9. P. Olmsted, O. Radulescu and C.-Y. Lu, *Journal of Rheology*, 2000, **44**, 257-275.
10. P.-G. de Gennes, *The Journal of Chemical Physics*, 1971, **55**, 572-579.
11. M. Doi and S. Edwards, *Journal of the Chemical Society, Faraday Transactions 2: Molecular and Chemical Physics*, 1978, **74**, 1802-1817.
12. M. Doi and S. F. Edwards, *The Theory of Polymer Dynamics*, Oxford University Press, 1988.
13. G. Marrucci, Grizzuti, N. , *Gazzetta Chimica Italiana*, 1988, **118**, 179–185.
14. G. Marrucci, *Journal of Non-Newtonian Fluid Mechanics*, 1996, **62**, 279-289.
15. D. Mead, R. Larson and M. Doi, *Macromolecules*, 1998, **31**, 7895-7914.
16. G. Ianniruberto and G. Marrucci, *Journal of Non-Newtonian Fluid Mechanics*, 2000, **95**, 363-374.
17. A. E. Likhtman, S. T. Milner and T. C. McLeish, *Physical Review Letters*, 2000, **85**, 4550.
18. G. Ianniruberto and G. Marrucci, *Journal of Rheology*, 2001, **45**, 1305-1318.
19. M. E. Cates, *The Journal of Physical Chemistry*, 1990, **94**, 371-375.
20. N. A. Spenley, M. E. Cates and T. C. B. McLeish, *Physical Review Letters*, 1993, **71**, 939-942.
21. P. Tapadia, S. Ravindranath and S.-Q. Wang, *Physical Review Letters*, 2006, **96**, 196001.
22. P. E. Boukany and S.-Q. Wang, *Journal of Rheology*, 2007, **51**, 217-233.
23. P. E. Boukany and S.-Q. Wang, *Macromolecules*, 2008, **41**, 1455-1464.
24. P. E. Boukany and S.-Q. Wang, *Journal of Rheology*, 2009, **53**, 73-83.
25. S.-Q. Wang, S. Ravindranath and P. Boukany, *Macromolecules*, 2011, **44**, 183-190.
26. P. Tapadia and S.-Q. Wang, *Macromolecules*, 2004, **37**, 9083-9095.
27. M. E. Helgeson, L. Porcar, C. Lopez-Barron and N. J. Wagner, *Physical Review Letters*, 2010, **105**, 084501.
28. A. K. Gurnon, C. Lopez-Barron, M. J. Wasbrough, L. Porcar and N. J. Wagner, *ACS Macro Letters*, 2014, **3**, 276-280.
29. S. M. Fielding and P. D. Olmsted, *Physical Review Letters*, 2003, **90**, 224501.
30. S. M. Fielding, *Physical review letters*, 2005, **95**, 134501.
31. S. M. Fielding, *Physical Review E*, 2007, **76**, 016311.
32. S. M. Fielding, *Physical review letters*, 2010, **104**, 198303.
33. J. Adams, S. M. Fielding and P. D. Olmsted, *Journal of Rheology*, 2011, **55**, 1007-1032.
34. R. L. Moorcroft and S. M. Fielding, *Physical Review Letters*, 2013, **110**, 086001.
35. R. L. Moorcroft and S. M. Fielding, *Journal of Rheology*, 2014, **58**, 103-147.

36. O. Radulescu, P. Olmsted, J. Decruppe, S. Lerouge, J.-F. Berret and G. Porte, *EPL (Europhysics Letters)*, 2003, **62**, 230.
37. J. Adams and P. D. Olmsted, *Physical Review Letters*, 2009, **102**, 067801.
38. S. Skorski and P. D. Olmsted, *Journal of Rheology*, 2011, **55**, 1219-1246.
39. S. Lerouge and P. D. Olmsted, *Frontiers in Physics*, 2020, **7**, 246.
40. M. Cromer, M. C. Villet, G. H. Fredrickson and L. G. Leal, *Physics of Fluids*, 2013, **25**, 051703.
41. Y. Wang and S.-Q. Wang, *arXiv preprint arXiv:1806.06159*, 2018.
42. J. Cao and A. E. Likhtman, *Physical Review Letters*, 2012, **108**, 028302.
43. M. Mohagheghi and B. Khomami, *ACS Macro Letters*, 2015, **4**, 684-688.
44. M. Mohagheghi and B. Khomami, *Physical Review E*, 2016, **93**, 062606.
45. M. Mohagheghi and B. Khomami, *Journal of Rheology*, 2016, **60**, 849-859.
46. M. H. Nafar Sefiddashti, B. J. Edwards and B. Khomami, *Polymers*, 2019, **11**, 476.
47. M. H. Nafar Sefiddashti, B. J. Edwards and B. Khomami, *Macromolecules*, 2019, **52**, 8124-8143.
48. M. H. Nafar Sefiddashti, M. Boudaghi Khajehnobar, B. J. Edwards and B. Khomami, *Scientific Reports*, 2020, **10**, 1-13.
49. P. J. Hoogerbrugge and J. M. V. A. Koelman, *EPL (Europhysics Letters)*, 1992, **19**, 155.
50. P. Español and P. B. Warren, *The Journal of Chemical Physics*, 2017, **146**, 150901.
51. P. Espanol and P. Warren, *EPL (Europhysics Letters)*, 1995, **30**, 191.
52. R. D. Groot and P. B. Warren, *The Journal of Chemical Physics*, 1997, **107**, 4423-4435.
53. P. Nikunen, I. Vattulainen and M. Karttunen, *Physical Review E*, 2007, **75**, 036713.
54. B. D. Todd and P. J. Daivis, *Nonequilibrium Molecular Dynamics: Theory, Algorithms and Applications*, Cambridge University Press, 2017.
55. J. Irving and J. G. Kirkwood, *The Journal of Chemical Physics*, 1950, **18**, 817-829.
56. M. Nafar Sefiddashti, B. J. Edwards and B. Khomami, *Journal of Rheology*, 2015, **59**, 119-153.
57. M. Nafar Sefiddashti, B. J. Edwards and B. Khomami, *Journal of Rheology*, 2016, **60**, 1227-1244.
58. M. H. N. Sefiddashti, B. J. Edwards and B. Khomami, *Physical Review Fluids*, 2017, **2**, 083301.
59. M. Kröger, *Computer Physics Communications*, 2005, **168**, 209-232.
60. R. S. Hoy, K. Foteinopoulou and M. Kröger, *Physical Review E*, 2009, **80**, 031803.
61. N. C. Karayiannis and M. Kröger, *International Journal of Molecular Sciences*, 2009, **10**, 5054-5089.
62. S. Shanbhag and M. Kröger, *Macromolecules*, 2007, **40**, 2897-2903.
63. J. Kim, B. J. Edwards, D. J. Keffer and B. Khomami, *Journal of Rheology*, 2010, **54**, 283-310.
64. A. E. Likhtman and T. C. McLeish, *Macromolecules*, 2002, **35**, 6332-6343.
65. D. J. Read, M. E. Shivokhin and A. E. Likhtman, *Journal of Rheology*, 2018, **62**, 1017-1036.
66. P. S. Stephanou, C. Baig and V. G. Mavrantzas, *Journal of Rheology*, 2009, **53**, 309-337.
67. J. Kim, P. S. Stephanou, B. J. Edwards and B. Khomami, *Journal of Non-Newtonian Fluid Mechanics*, 2011, **166**, 593-606.
68. S. Wasserman and W. Graessley, *Journal of Rheology*, 1992, **36**, 543-572.

69. J. Kim, B. J. Edwards, D. J. Keffer and B. Khomami, *Physics Letters A*, 2009, **373**, 769-772.
70. C. Baig, V. G. Mavrantzas and M. Kroger, *Macromolecules*, 2010, **43**, 6886-6902.
71. F. A. Morrison, *Understanding Rheology*, Oxford University Press, USA, 2001.
72. R. B. Bird, R. C. Armstrong and O. Hassager, *Dynamics of Polymeric Liquids: Fluid Mechanics*, John Wiley and Sons Inc., New York, NY (USA), 1987.
73. R. G. Larson, *The Structure and Rheology of Complex Fluids*, Oxford University Press, New York, 1999.
74. J. M. Dealy, D. J. Read and R. G. Larson, *Structure and Rheology of Molten Polymers: from Structure to Flow Behavior and back again*, Carl Hanser Verlag GmbH Co KG, 2018.

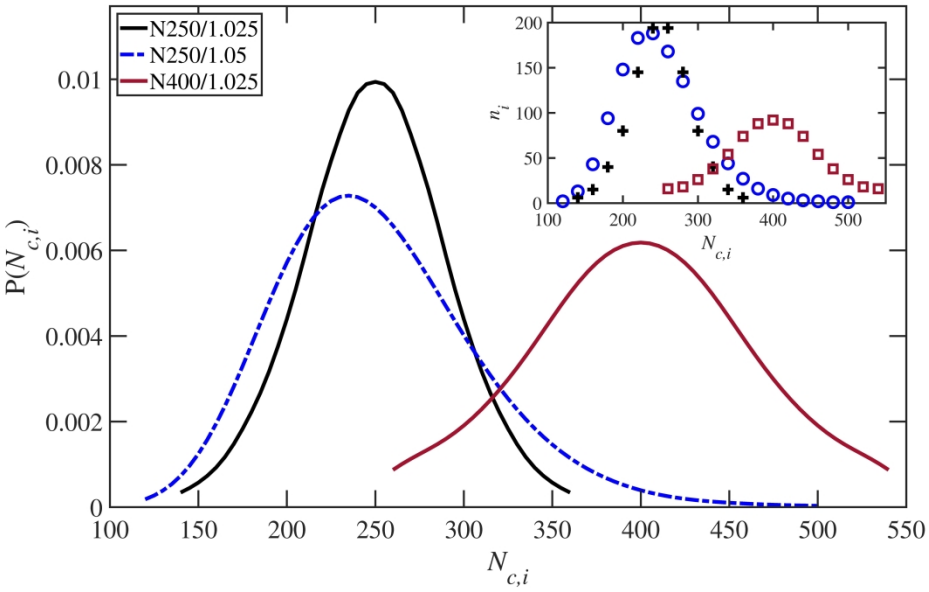

Figure 1

385x257mm (300 x 300 DPI)

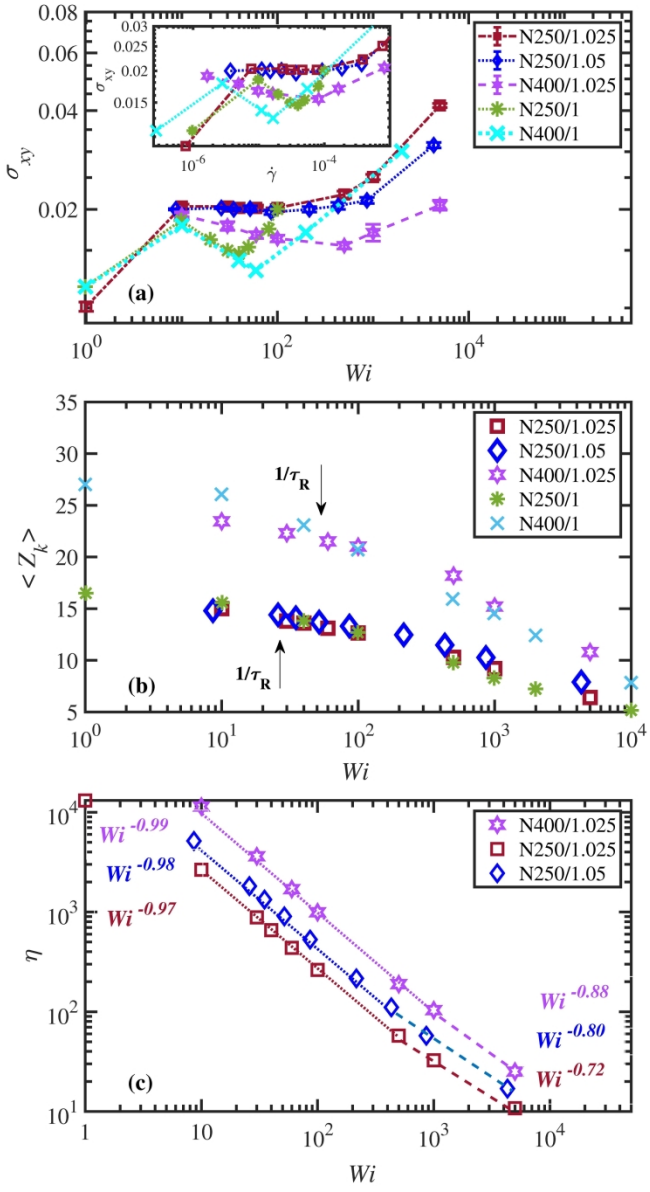

Figure 2

202x334mm (300 x 300 DPI)

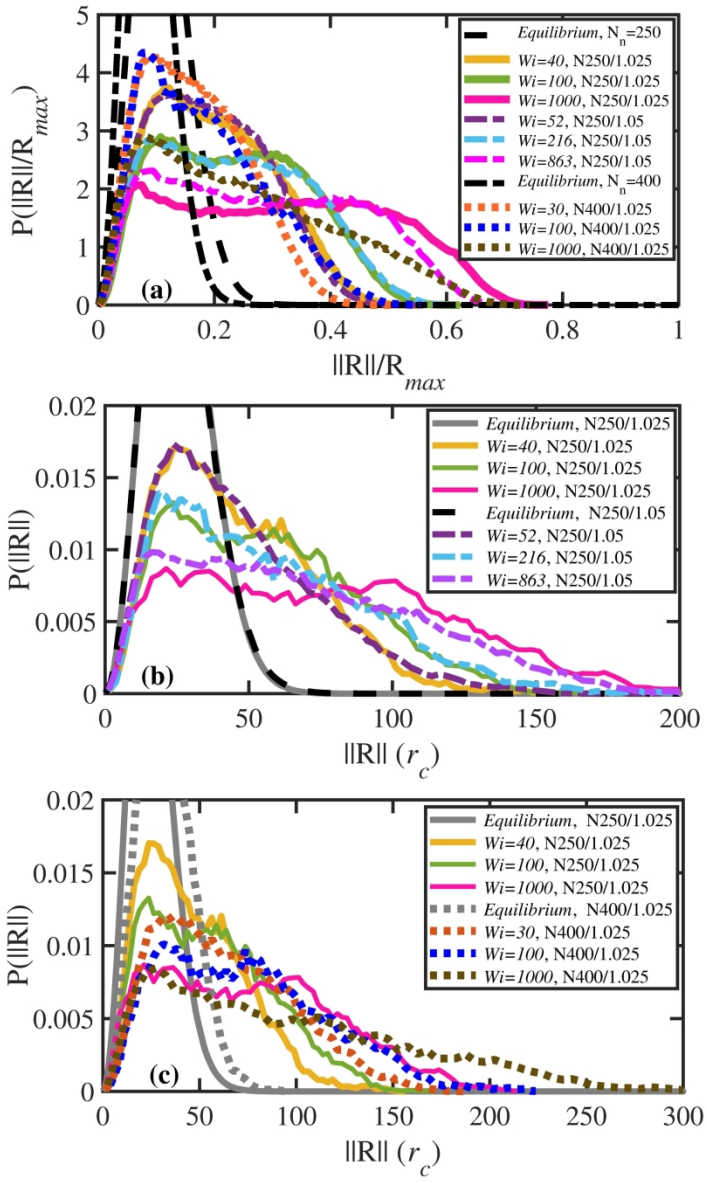

Figure 3

166x277mm (300 x 300 DPI)

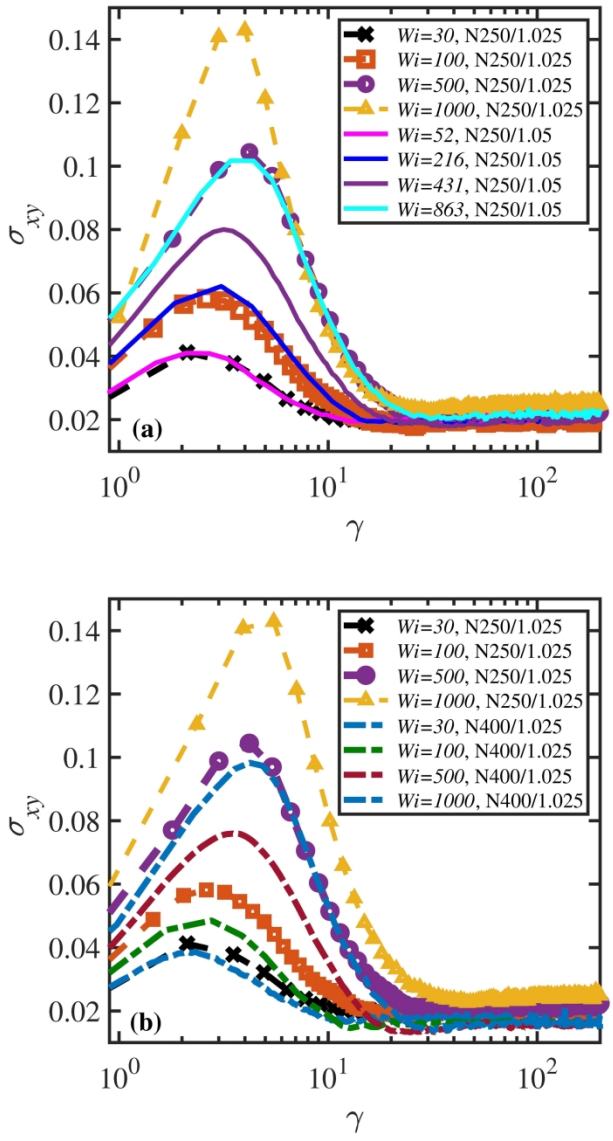

Figure 4

157x286mm (300 x 300 DPI)

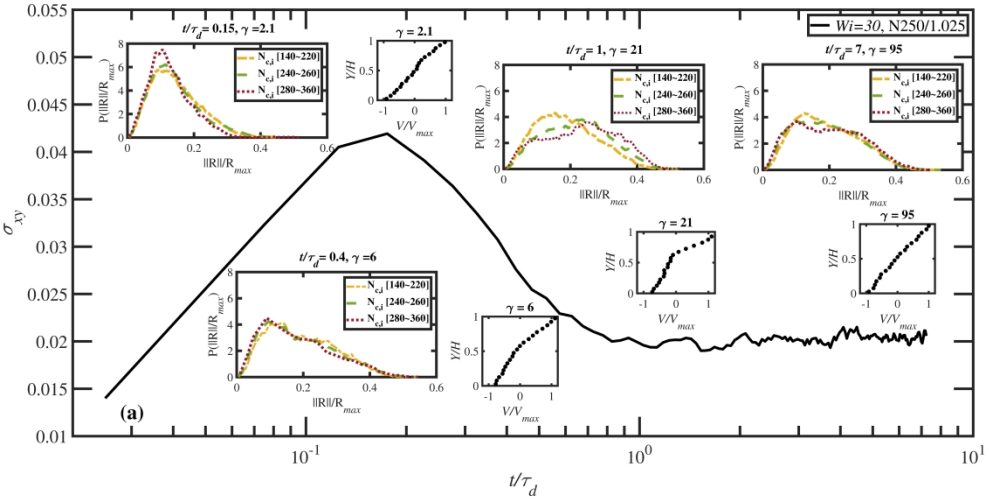

Figure 5(a)

547x291mm (300 x 300 DPI)

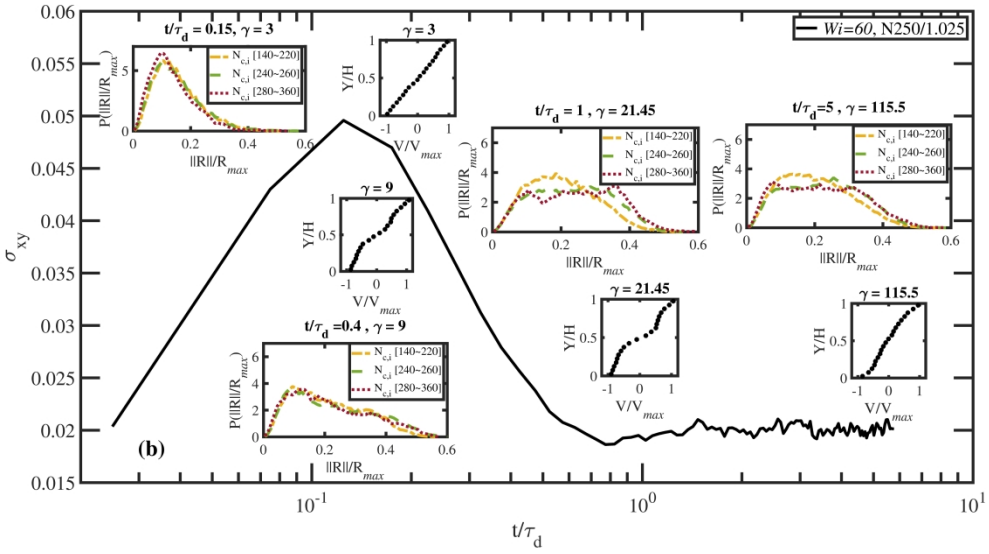

Figure 5(b)

503x286mm (300 x 300 DPI)

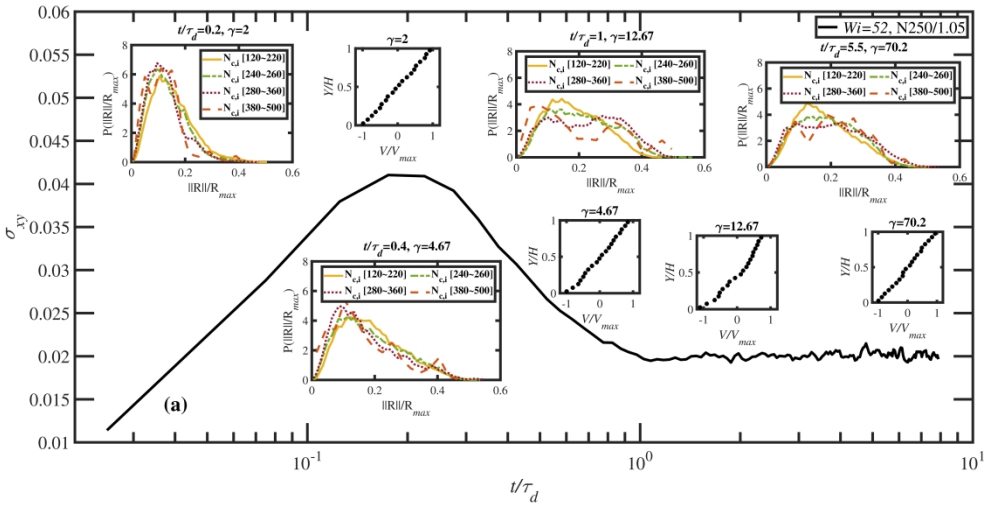

Figure 6(a)

547x291mm (300 x 300 DPI)

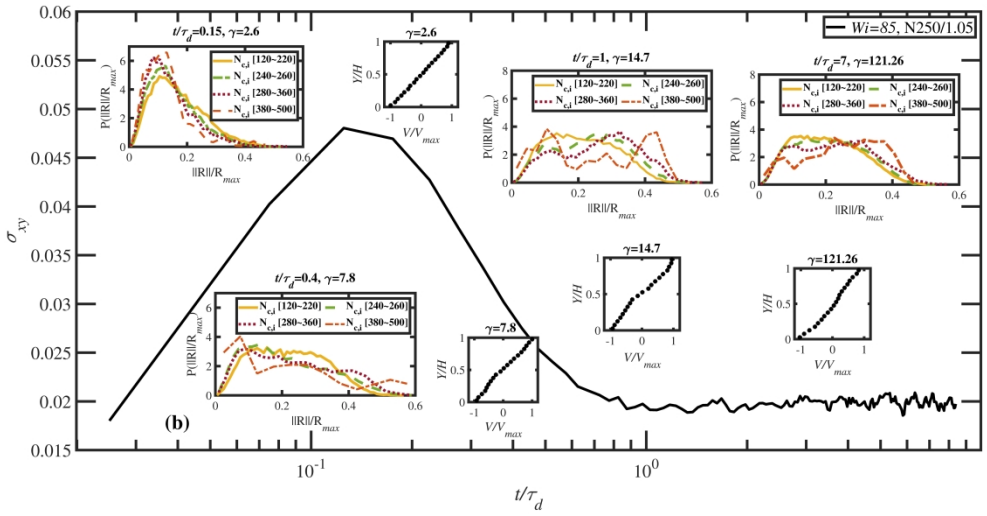

Figure 6(b)

546x290mm (300 x 300 DPI)

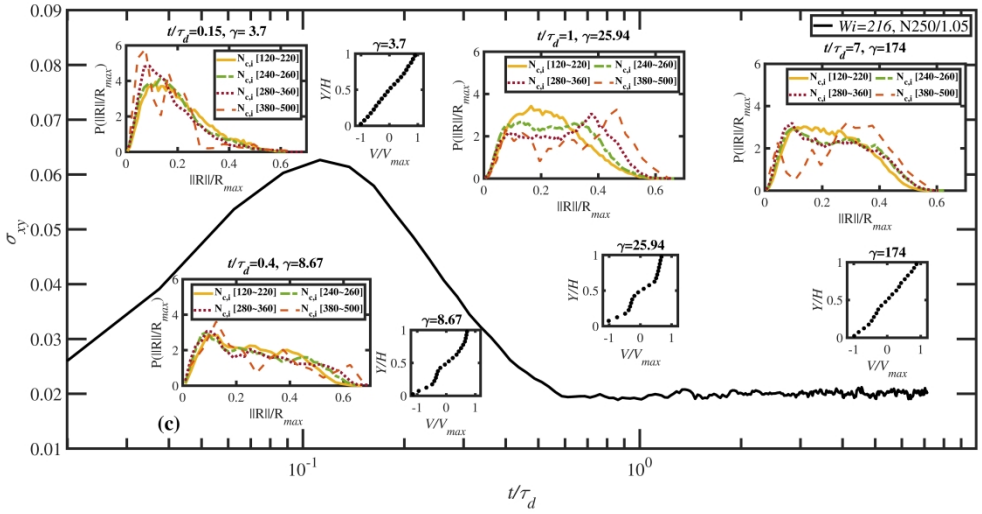

Figure 6(c)

547x291mm (300 x 300 DPI)

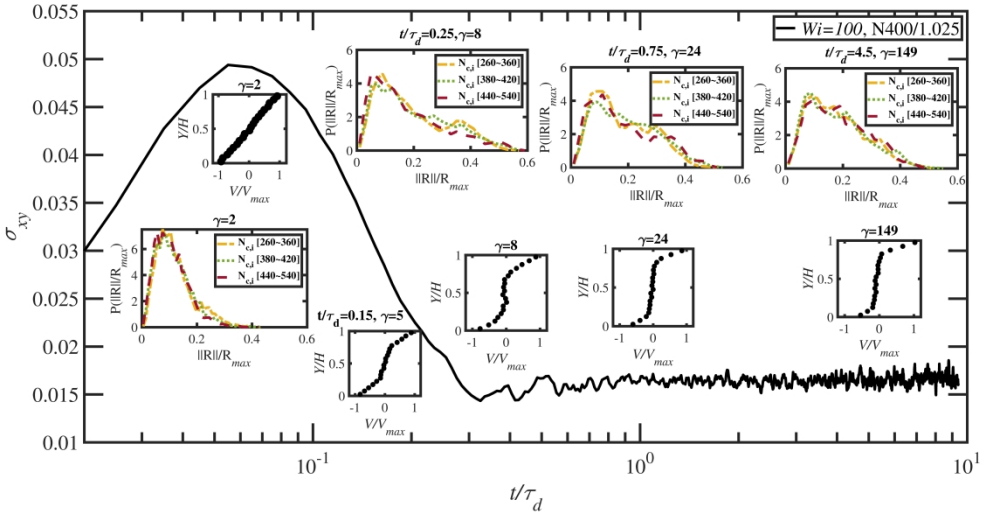

Figure 7

547x290mm (300 x 300 DPI)

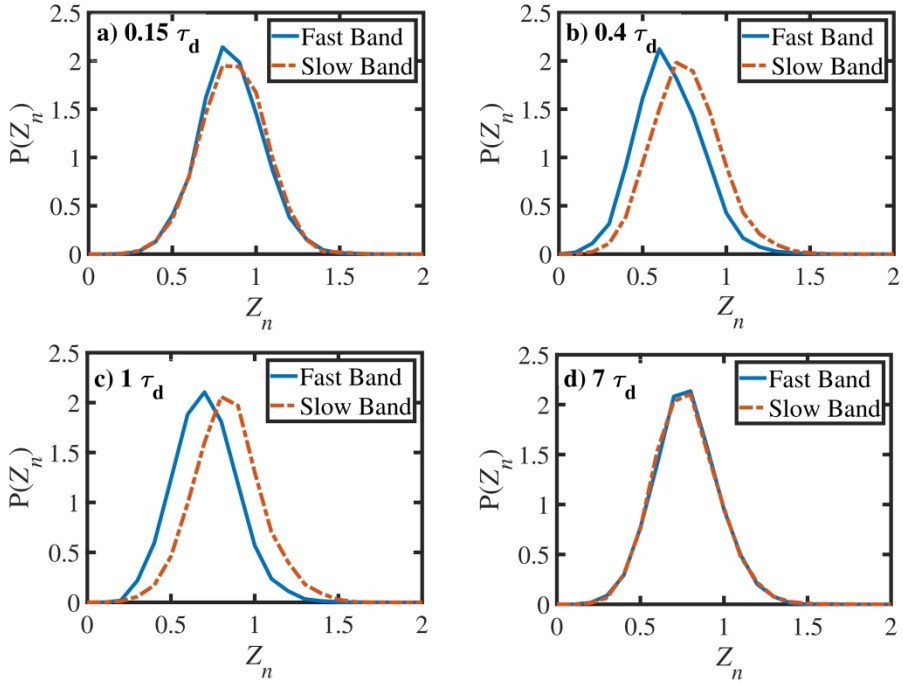

Figure 8

388x284mm (300 x 300 DPI)

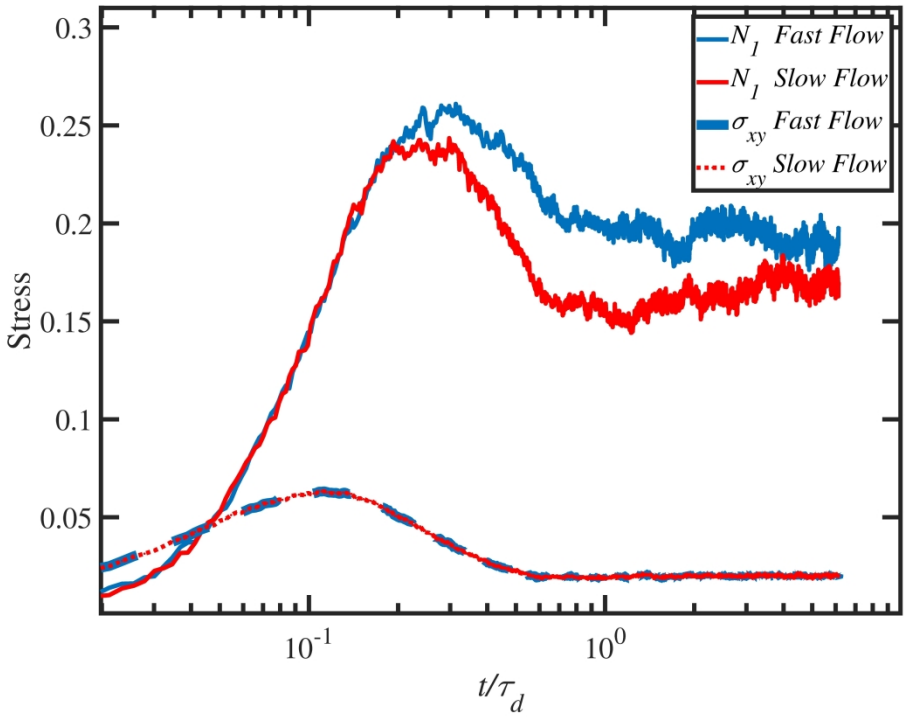

Figure 9

330x250mm (300 x 300 DPI)

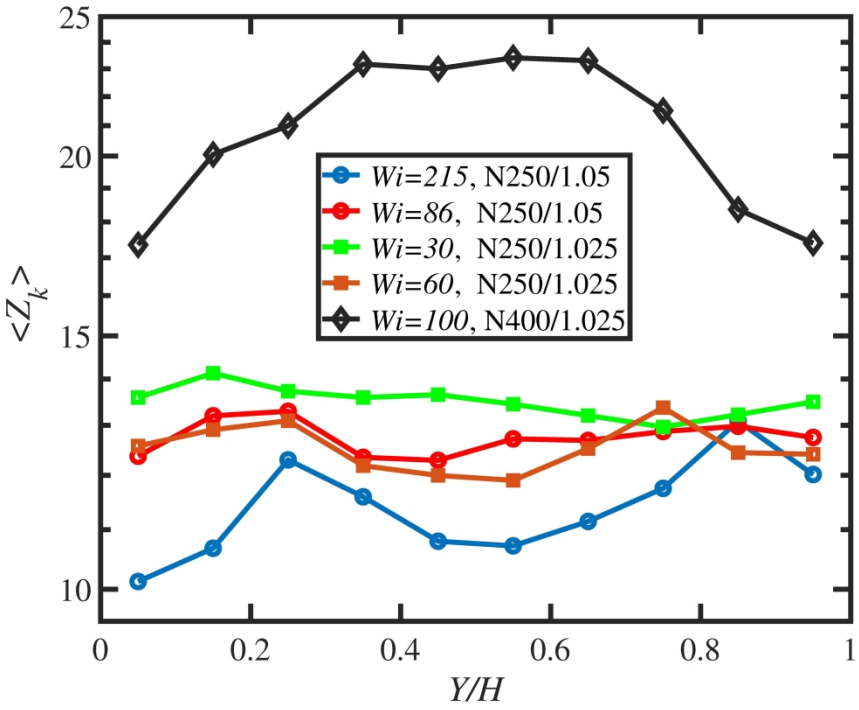

Figure 10

282x213mm (300 x 300 DPI)

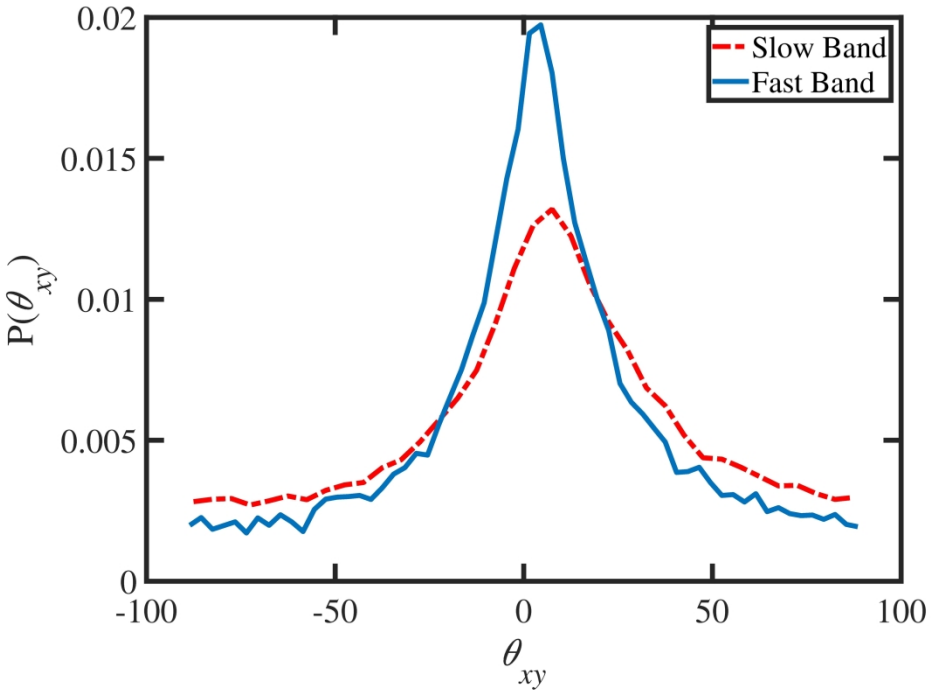

Figure 11

290x216mm (300 x 300 DPI)

Table of Contents Entry

Transient and steady-state shear banding are demonstrated for polydisperse polymer melts as functions of applied shear rate.